Journal of Materials Chemistry C

ROYAL SOCIETY OF CHEMISTRY

PAPER

View Article Online
View Journal | View Issue

Cite this: J. Mater. Chem. C, 2021, 9, 1025

Ampholytic interface induced *in situ* growth of $CsPbBr_3$ for highly efficient perovskite light-emitting diodes†

Jianfeng Ou,[ab] Xiaoyang Guo, *[a] Li Song, [c] Jie Lin, [a] Ying Lv, [a] Yi Fan,[a] Yantao Li,[a] Deyue Zou,[ab] Zhiqiang Bao[ab] and Xingyuan Liu *[a]

Morphology has important effects on the performance and working stability of metal halide perovskite optoelectronic devices. It is widely believed that a uniform and pinhole-free perovskite film with closely arranged small grains is an ideal morphology for realizing high electroluminescence (EL) efficiency. This work presents an ethanolamine (EA) interface for *in situ* induction of perovskite nucleation and growth. Meanwhile a Lewis base of Tween 80 (T80) is employed as the defect passivator to suppress the defects in the bulk film. Under the combined effect of EA and T80, the optimal luminescence device displays a low opening voltage of 2.4 V, a peak current efficiency of 44.32 cd A^{-1}, a maximum external quantum efficiency of 12.7%, a maximum brightness of 50 900 cd m^{-2}, and a prolonged operational lifetime of 4.5 h. The detailed investigation reveals the mechanism of the effect of the EA interface. The EA can interact with both the hole transporting layer poly(ethylenedioxythiophene):polystyrenesulfonate (PEDOT:PSS) and the perovskite emissive layer $CsPbBr_3$ together, acting as a connecting agent due to its special functional groups of hydroxyl and amine, thus inducing grain nucleation and growth. As a result, a compact and pinhole-free perovskite film was obtained by the introduction of EA. This work will give beneficial insight for *in situ* morphology control of perovskite grains.

Received 13th November 2020,
Accepted 9th December 2020

DOI: 10.1039/d0tc05335j

rsc.li/materials-c

Introduction

Metal halide perovskite materials are a new type of photoelectric material with a high absorption coefficient,[1,2] long carrier diffusion length,[3,4] high mobility,[5] and the advantages of tunable band gap,[6,7] which have received widespread attention for application in solar cells,[8,9] photodetectors,[10–12] light-emitting diodes,[13,14] and lasers.[15–18] Moreover, the novel characteristics of perovskite materials provide opportunities for innovation and new device structure design.[19,20] In particular, since the first room temperature emission was realized in 2014, the external quantum efficiency (EQE) of perovskite light-emitting diodes (PeLEDs) has exceeded 20% from the initial 0.1%.[21–23] Meanwhile, the operational stability of the device has also been greatly improved, which makes the PeLEDs hold great promise in the field of display.[24–27]

Morphology has important effects on the performance and working stability of metal halide perovskite optoelectronic devices.[28–30] It is generally believed that the uniform and pinhole-free perovskite film with closely arranged small grains is an ideal morphology for realizing high electroluminescence (EL) efficiency.[31,32] However, in the perovskite device prepared by solution method, the different solubilities of the perovskite precursor in polar media (such as dimethyl formamide and dimethyl sulfoxide), the diversity of ions in the solution and uncontrollable crystallization of the perovskite solution in the process of spin coating can lead to the formation of the defects. In particular, in the inorganic $CsPbBr_3$ system with limited solubility, formation of many pin-holes between large perovskite grains occurs, inducing leakage currents and shunt paths during the process of charge injection, which may further lower the charge capture efficiency, and increase Joule heating in PeLEDs, thus limiting the EL performance. To reduce the formation of pin-holes, one effective strategy is introducing passivation agents into the perovskite precursor solution, such as Lewis acids, Lewis bases, metal cations, organic cations,[33] *etc.* The defects at the grain boundaries had been suppressed to different degrees by those passivators, but in the meanwhile the

[a] State Key Laboratory of Luminescence and Applications, Changchun Institute of Optics, Fine Mechanics and Physics, Chinese Academy of Sciences, Changchun 130033, China
[b] University of Chinese Academy of Sciences, Beijing 100049, China
[c] Tianjin Key Laboratory of Electronic Materials and Devices, School of Electronics and Information Engineering, Hebei University of Technology, 5340 Xiping Road, Tianjin 300401, P. R. China

† Electronic supplementary information (ESI) available. See DOI: 10.1039/d0tc05335j

discontinuous perovskite films with large grain size were usually achieved, which may require a thicker carrier transporting layer to avoid a short circuit and ensure a low current shunt.[34,35] However, the thick interfacial layer with poor conductance would lead to an increase in the device internal resistance, causing increased turn-on voltage and lowered device efficiency. Therefore, during passivation, morphology control in $CsPbBr_3$ interface to induce the crystal nucleus formation and crystal growth is also of great importance to regulate the process dynamics of carrier transmission and recombination.

It is well known that the number of crystal nuclei determines the size and number of grains in the film during the crystallization process. So the bottom interface of the perovskite layer not only acts as a charge transport/injection layer, but also plays a role in adjusting the crystallization process.[36–40] In previous studies, several inorganic metal oxides, organic or organic/inorganic composite interfacial layers have been employed in PeLEDs to control the morphologies of perovskite films, for example, a thin atomic layer-deposited aluminum oxide (Al_2O_3) layer below the perovskite layer can improve the interfacial contact, enhance EL characteristics and balance charge injection;[41] highly polar lithium fluoride (LiF) can act as an effective template for forming high-quality bromide perovskites;[42] polyethyleneimine (PEI) and polyethyleneimine ethoxylated (PEIE) can enhance the crystallinity and surface coverage of perovskite films;[43,44] poly(9-vinylcarbazole) (PVK): 2-((4-biphenylyl)-5-phenyl-1,3,4-oxadiazole) (PBD) can enhance the interfacial quality by removing pinholes and decreasing the roughness of the perovskite layers;[45] diamine molecule [2,2-(ethyndioxy)bis(ethyl ammonium), EDBE] can be used as the modification layer of electron transport layer and perovskite layer, which can obtain high-quality perovskite thin films and promote electron injection, thus realizing high-performance near-infrared light-emitting diodes.[46] In addition, directly doping polar molecules into PEDOT:PSS can also promote perovskite crystallization and inhibit defect-induced nonradiative recombination.[47,48] But most of those interfacial materials also have some specific disadvantages, for example, metal oxides have quite fixed energy levels, and require high-vacuum fabrication, or a high-temperature process.[49,50] And organic interfacial materials usually have low conductivity and poor compatibility with perovskites.[51,52] Although the use of organic/inorganic composite materials have overcome some drawbacks of inorganic or organic interfaces, the introduction of new interface problems and interface control mechanism still needs further research.[34,53,54] Therefore, design and investigation of the appropriate interfacial layers and revealing the underlying mechanisms is necessary to develop highly efficient PeLEDs.

In this study, an ampholytic interface ethanolamine (EA) was inserted between the hole transporting layer of poly(ethylenedioxythiophene):polystyrenesulfonate (PEDOT:PSS) and the perovskite emissive layer to induce *in situ* growth of $CsPbBr_3$ crystals. At the same time, a Lewis base of Tween 80 (T80) with multiple hydroxyl was selected as the additive to suppress the formation of the non-radiative traps by passivating the defective states in the bulk perovskite. As a result, a compact and uniform morphology was obtained by increasing the *in situ* nucleation, and an enhanced device performance was also achieved, including a peak current efficiency (CE) of 44.32 cd A^{-1}, and a peak EQE of 12.70%. Meanwhile, the operational lifetime of the modified device without encapsulation was also improved to about 4.5 h, which is much higher than that of the control device. The mechanism of the ampholytic interface in $CsPbBr_3$ based PeLEDs was finally discussed, which reveals the method of the *in situ* nucleus formation and growth of the grains.

Results and discussion

In this work, a traditional PeLED structure was utilized to fabricate the $CsPbBr_3$ based PeLEDs. Fig. 1a shows the schematic device structure of ITO/PEDOT:PSS/EA/$CsPbBr_3$/TPBi/Bphen/Cs_2CO_3/Ag and the corresponding cross-sectional scanning electron microscopy (SEM) image is shown in Fig. 1b. According to previous reports, additives with hydroxyl functional groups would help to passivate the defect sites of Pb^{2+} vacancies.[55,56] So here T80 with a multi-hydroxyl molecular structure (Fig. 1c) was employed in the perovskite film to suppress the non-radiative recombination in the perovskite luminescent layer. Meanwhile, an ampholytic molecular EA with both amine and hydroxyl groups was inserted between PEDOT:PSS and $CsPbBr_3$. Fig. 1d–g shows the EL characteristics of the current density–voltage–luminance (*J–V–L*), CE–voltage (CE–V), and EQE–voltage (EQE–V) curves the PeLEDs with different treatments and the EL parameters are listed in Table 1. For the control PeLED, it exhibits quite a poor performance with a maximum luminance of 3980 cd m^{-2}, a maximum CE of 2.88 cd A^{-1}, a maximum EQE of 0.87%, and a pretty high turn-on voltage (V_{on}) of 2.73 V, respectively. While the perovskite layer was treated by EA at the bottom interface or T80 (5 mg ml^{-1}) in the precursor solution, the EL performance of the PeLEDs have been improved to different degrees, the maximum CEs are 14.4 and 28.2 cd A^{-1}, the maximum EQEs are 4.34 and 8.12%, and the V_{on} are lowered to 2.62 and 2.43 V, respectively. It is also worth pointing out that the devices were fabricated under the optimized condition, and the detailed information of previous treated methods is shown in Fig. S1–S4 (ESI†). As both of the treatments act together on one PeLED, the EL characteristics are further enhanced, displaying a maximum brightness of 50 900 cd m^{-2}, a maximum CE of 44.32 cd A^{-1}, a maximum EQE of 12.7%, and a low V_{on} of 2.41 V, confirming the effect of the EA interface and T80 addition on the $CsPbBr_3$ based PeLEDs. The EL spectra of the PeLEDs with different treatments are shown in Fig. 1g. It is found that the two EL spectra of the device with T80 treated only and the device with EA and T80 treated together display a peak centered at about 521 nm with a full width at half maximum (FWHM) of 18 nm and no obvious peak drift as the bias increased from 3 V to 5 V (Fig. S5, ESI†). These two spectra exhibit EL red-shift compared with the other two devices with the neat $CsPbBr_3$ and EA modified $CsPbBr_3$, which probably originates from the grain boundary changes induced by T80.[14] The EL spectra of neat $CsPbBr_3$ and EA

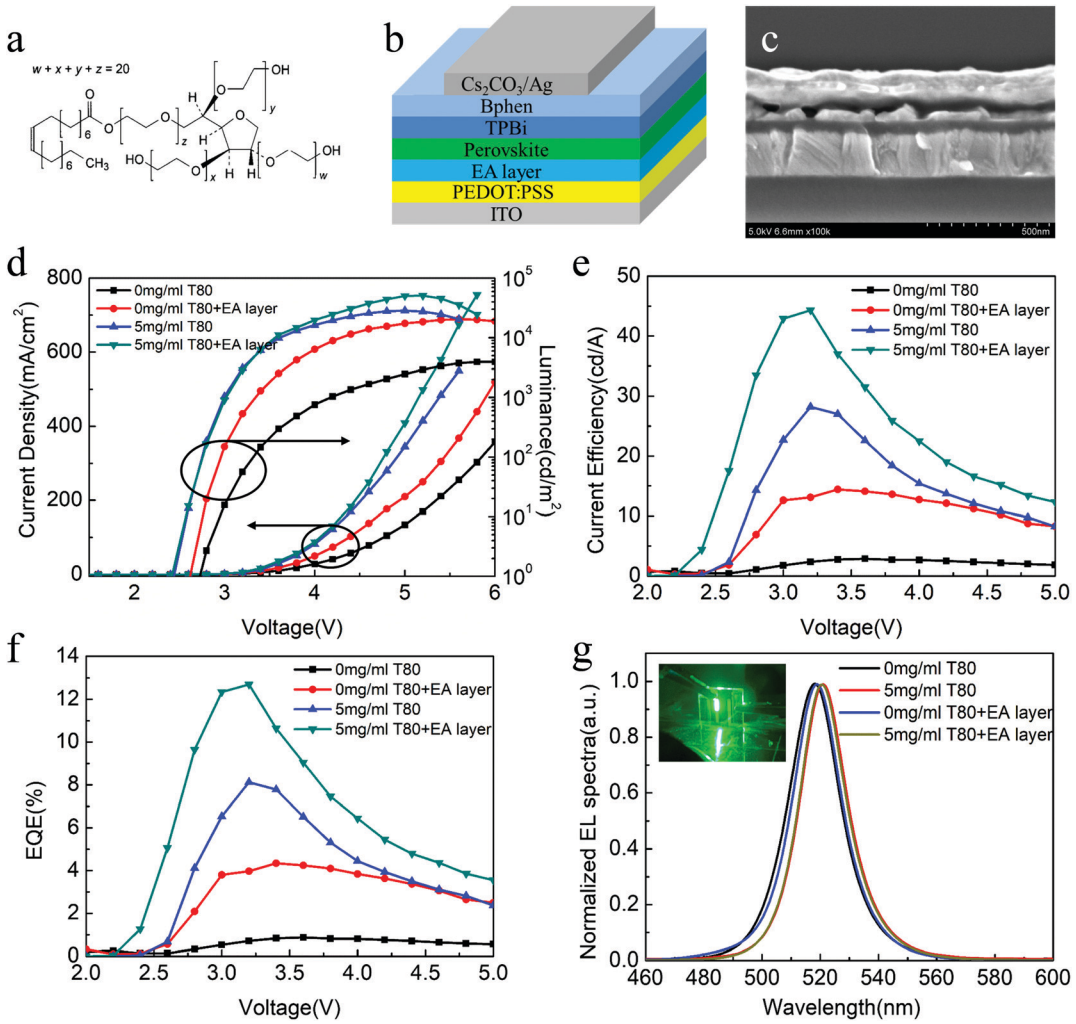

Fig. 1 (a) Schematic representation and (b) cross-sectional SEM image of $CsPbBr_3$ PeLED. (c) Molecule structure of T80. (d) *J*–*V*–*L*, (e) CE–*V*, and (f) EQE–*V* curves for the PeLEDs. (g) EL spectra of various devices working at 4.0 V. (inset: Photograph of the optimal PeLED under applied voltages of 4.0 V.)

modified $CsPbBr_3$ devices are almost the same, implying that the EA interlayer does not change the recombination zone.[46] A photo of the operating device is shown in the inset of Fig. 1g. In addition, as shown in Fig. S6 (ESI†), the optimized PeLED emits green light with Commission Internationale de l'Eclairage (CIE) coordinates of (0.122, 0.780).

Fig. 2a showed the optical properties of perovskite films under the different treatments. Photoluminescence (PL) peaks of the two $CsPbBr_3$ films without T80 addition were located at about 519 nm, while the other two PL peaks of $CsPbBr_3$ film doped by T80 were at about 524 nm, suggesting obvious red-shifted spectra under the action of T80. This is consistent with the trend of the EL spectra (Fig. 1g). X-ray diffraction patterns (Fig. S7, ESI†) demonstrate that the crystal structure of $CsPbBr_3$ is not affected by T80 and the EA layer because no difference in the XRD diffraction peaks is observed except for the weakened diffraction intensity, which excludes the impact by lattice strain. Fig. 2a also displays the PL images of neat $CsPbBr_3$, $CsPbBr_3$ + EA, $CsPbBr_3$ + T80, and $CsPbBr_3$ + EA + T80 films, which shows the trend of the brightness enhancement and the corresponding PL quantum yields (PLQYs) of these films are 1.3%, 5.6%, 16.3%, and 19.7%, respectively, indicating that the EA interface layer together with the T80 passivator can inhibit the non-radiative recombination in the $CsPbBr_3$ film by reducing defect formation.

Table 1 EL performance of the $CsPbBr_3$ PeLEDs with different treatments (with/without T80 and with/without the EA layer)

EA (with/without)	T80 (mg ml^{-1})	L_{Max} (cd m^{-2})	CE_{Max} (cd A^{-1})	EQE_{Max} (%)	V_{on} (V)
without	0	3980	2.88	0.87	2.73
with	0	20 500	14.40	4.34	2.62
without	5	28 600	28.20	8.12	2.43
with	5	50 900	44.32	12.70	2.41

In order to understand the carrier dynamics in the perovskite film, the time-resolved PL decay of the perovskite film was also studied, as shown in Fig. 2b. It is seen that compared with the neat $CsPbBr_3$ film, the carrier lifetimes of the modified films were significantly extended. The average PL lifetimes of neat $CsPbBr_3$, $CsPbBr_3$ + EA, $CsPbBr_3$ + T80, and $CsPbBr_3$ + EA +

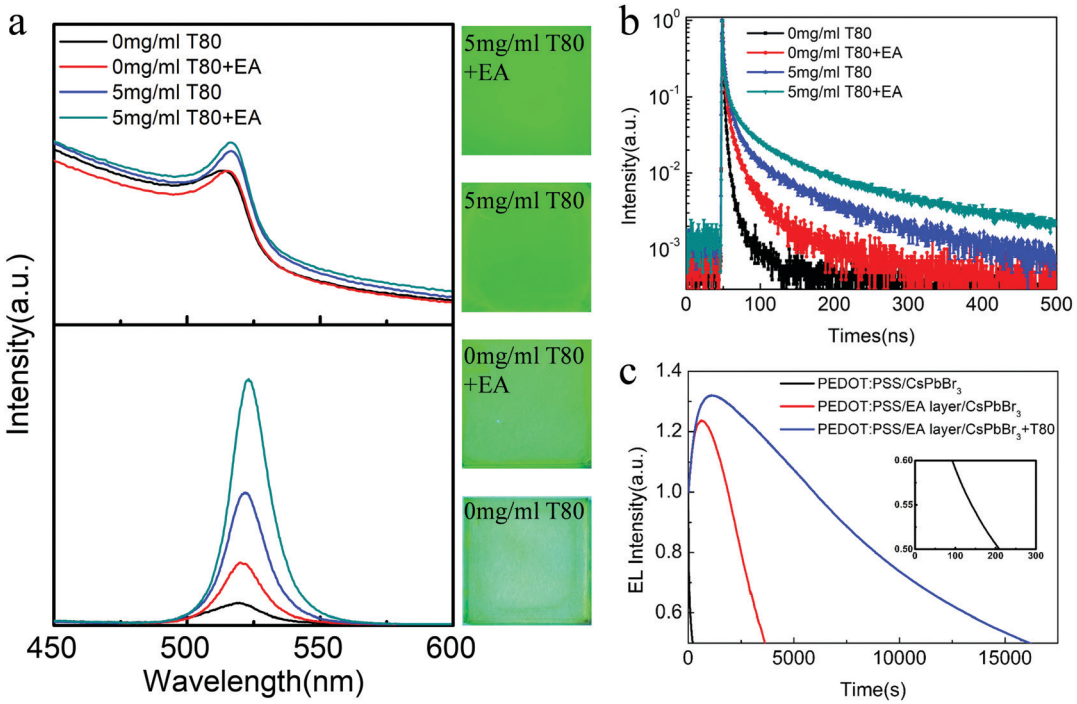

Fig. 2 (a) Absorption and PL spectra of $CsPbBr_3$ perovskite thin films on ITO substrates. Insets: PL images of the $CsPbBr_3$ perovskite films under ultraviolet lamp excitation (Hg lamp, 365 nm). (b) Time-resolved PL decay curves of $CsPbBr_3$ perovskite films measured under the excitation of 380 nm. (c) Operational lifetime of PeLEDs based on PEDOT:PSS/$CsPbBr_3$, PEDOT:PSS/EA/$CsPbBr_3$, and PEDOT:PSS/EA/$CsPbBr_3$ +T80 (L_0 = 100 cd m^{-2}).

T80 films are 4.89, 12.97, 30.27, and 48.94 ns, respectively (Table S1, ESI†). To provide further insight into the effect of these methods on the defect suppression, the non-radiative recombination rate of these films are calculated. As the radiative and non-radiative recombination rates are related to the average PL lifetime τ_{avg} and PLQY:

$$\tau_{avg} = \frac{1}{k_r + k_{nr}}$$

$$PLQY = \frac{k_r}{k_r + k_{nr}}$$

where k_r and k_{nr} represent the radiative and non-radiative recombination rate, respectively; the non-radiative recombination rate can be calculated as

$$k_{nr} = \frac{1 - PLQY}{\tau_{avg}}$$

Obviously, the non-radiative recombination rate of the film is inversely proportional to its PLQY and τ_{avg}. Therefore, a higher PLQY and a longer average PL life of the $CsPbBr_3$ film would achieve a lower non-radiative recombination rate. The calculated non-radiative recombination rates of the neat $CsPbBr_3$, $CsPbBr_3$ + EA, and $CsPbBr_3$ + T80 films are 2.0×10^8, 7.3×10^7, and 3.4×10^7 s^{-1}, respectively. When the $CsPbBr_3$ film was treated by both EA and T80, the value of the non-radiative recombination rate is further decreased to 2.2×10^7 s^{-1}, which is one order of magnitude lower than that of the reference sample, indicating the effect of EA and T80 on suppressing the non-radiative defects. As a result, the optimized device exhibits a prolonged operational lifetime compared with the reference device, and Fig. 2c shows the operational lifetime of PeLED devices with different treatments. For the pure $CsPbBr_3$ based device, the brightness of the device was reduced to half of the initial value after only 3 min of continuous operation. This is mainly because serious non-radiative recombination occured in the pure $CsPbBr_3$ thin film caused by a lot of defects. Because of the addition of the EA interface layer between the hole transporting layer and the perovskite luminescent layer to modify the interfacial defects, the operational lifetime of the device prolonged to 1h. On this basis, the T80 doping into the perovskite luminescent layer can further passivate the defect states in the perovskite thin film and reduce the non-radiative recombination in the bulk. And the operational lifetime of PeLEDs further increased to 4.5 h, proving the synergistic effect of EA and T80 on enhancing the stability of $CsPbBr_3$ based PeLEDs.[57,58]

In order to investigate the effect of the above treatments on the morphology of the perovskite film, SEM and atomic force microscopy (AFM) of perovskite films were used to characterize the perovskite films, as shown in Fig. 3(a–h), and the grain size distribution of perovskite films is calculated according to AFM images, and the statistical results are shown in Fig. 3(i–l). It was found that the morphology of perovskite films changed significantly after the addition of the EA interface layer. As seen in Fig. 3a, the pure $CsPbBr_3$ film displays low coverage and many pin-holes, causing a poor EL performance in the corresponding device. However, the addition of the EA interface improved the continuity of the thin film (Fig. 3b), significantly decreased the

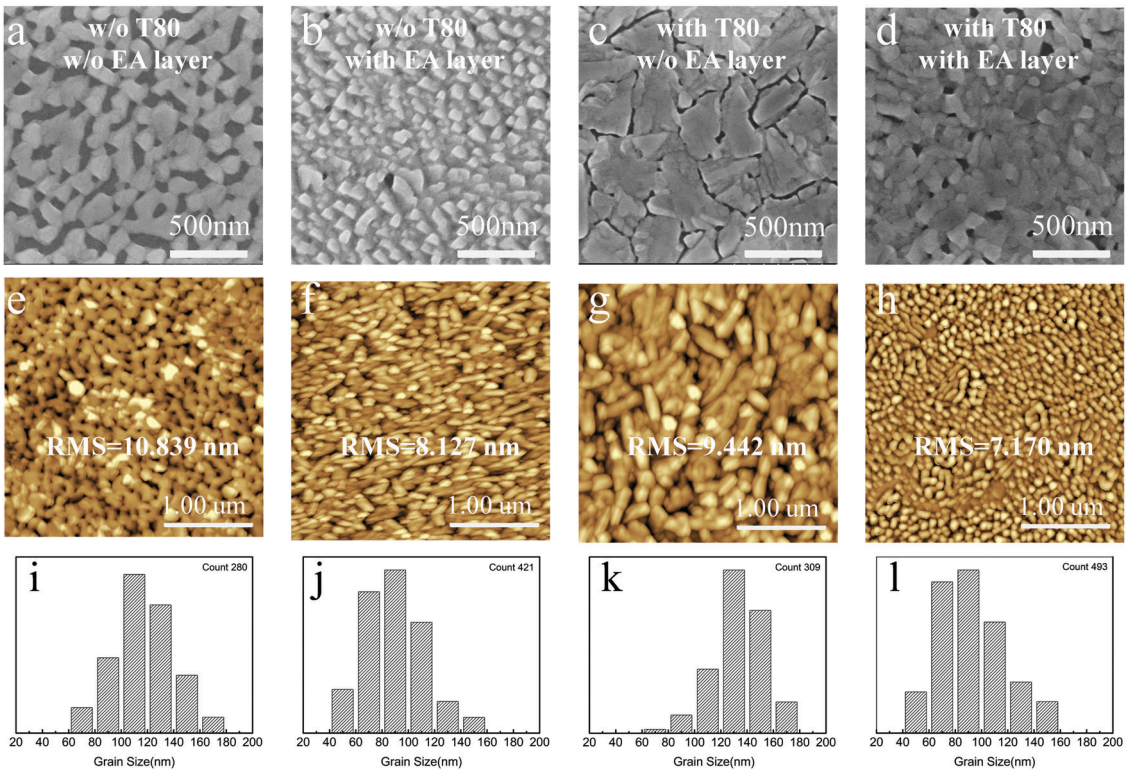

Fig. 3 SEM images (a)–(d) AFM images (e)–(h) and grain size distribution (i)–(l) of perovskite films under different conditions.

grain size (Fig. 3j) and increased the number of grains, and smoothed the perovskite film. The mean square roughness (RMS) of the EA treated film is 8.127 nm (Fig. 3e), much flatter than the pure $CsPbBr_3$ film (10.839 nm, Fig. 3f). For the perovskite film doped by T80 only (Fig. 3c), the grains agglomerated into large sheets, similar to the previous studies,[14] T80 in the form of a passivator, exists among perovskite grains and passivate non-radiation composite defects mainly by bonding small perovskite grains into large grains (Fig. 3k). But when the EA interface was introduced into the T80 treated $CsPbBr_3$ film (Fig. 3d), the grain phase morphology changed from aggregation to decentralization with uniform grain size (Fig. 3d and l), and the RMS further decreased from 9.442 nm (Fig. 3g) to 7.17 nm (Fig. 3h), indicating that the EA interface layer has the advantage of inducing *in situ* nucleation and growth of $CsPbBr_3$ grains.[59] We also quantitatively analyzed the trap density in perovskite thin films under different conditions, which further proved that adding T80 into the perovskite and EA interface layer can effectively passivate defects in perovskite thin films. We measured the dark current of hole-only devices with the ITO/PEDOT: PSS/perovskite/MoO_3/Ag structure under different bias voltages, and calculated the trap density using the following equation:

$$n_t = \frac{2\varepsilon_0\varepsilon_r V_{TFL}}{qL^2}$$

where ε_0 and ε_r are the vacuum permittivity and relative dielectric constant, q is the elemental charge, L is the thickness of perovskite film, and V_{TFL} is the onset voltage of the trap-filled limit region. V_{TFL} was calculated from the intersection of two tangents as shown in Fig. S8 (ESI†) at the low voltages and trap-filling regions.[14,60,61] As shown in Table S2 (ESI†), the hole trap densities of T80 and EA treated perovskite films are 1.56×10^{17} cm^{-3} and 2.43×10^{17} cm^{-3}, respectively, which both are significantly lower than that of the control device (3.95×10^{17} cm^{-3}). When T80 and EA act at the same time, the trap density of perovskite thin films is further decreased to 1.05×10^{17} cm^{-3}, which indicates that the synergistic effect of T80 and EA can effectively reduce the trap states in the perovskite films.

To better reveal the mechanism under the changingmorphology contact angle measurements have been obtained, which show that perovskite precursor solution had better wettability on the EA treated interface layer (Fig. S9, ESI†). The contact angle of the $CsPbBr_3$ precursor solution on the PEDOT:PSS film was about 22.81°, while the value decreased to 18.04° for the film deposited on the EA interface layer, and to 19.63° for the film doped by T80. And the contact angle further reduced to 15.02° for the film treated by both of EA and T80, illustrating that the EA interface made the film wettability better and thus significantly affected the contact angle. It is well known that the relationship between the energy required for crystal nucleation and contact angle (θ) can be described as follows:

$$\Delta G_{heterogenous} = \Delta G_{homogenous} \times f(\theta)$$

$$f(\theta) = \frac{1}{4}(1 - \cos\theta)^2(2 + \cos\theta)$$

$\Delta G_{heterogenous}$ and $\Delta G_{homogenous}$ represent the free energy

required for heterogeneous nucleation and homogeneous nucleation, respectively. According to this nucleation theory, a small contact angle would have been more advantageous to reduce the heterogeneous nucleation energy, and make the nucleation easier, thus forming a compact and uniform morphology as discussed above (Fig. 3).[43]

It is worth noting that although the contact angle of $CsPbBr_3$ film was also decreased by doping T80, the grain morphology of this film is very different compared with the EA modified $CsPbBr_3$ film. We deduced that the main reason for this is attributed to the ampholytic EA interface, which has special functional groups of hydroxyl and amine. In previous research studies, amine groups were found to tend to coordinate with sulfonyl groups in PEDOT:PSS, while hydroxyl groups interacted strongly with lead ions in perovskites.[59] Therefore, the ampholytic EA would serve as a bridge to link the perovskite and PEDOT:PSS layers, and hydroxyl groups in EA would act as nucleation centers of perovskite crystals by absorbing lead ions, and promoting perovskite nucleation and growth.[55,56] The schematic diagram of the action mechanism of the EA interface layer is displayed in Fig. 4a. And to confirm the above mechanism, X-ray photoelectron spectroscopy (XPS) measurements were used

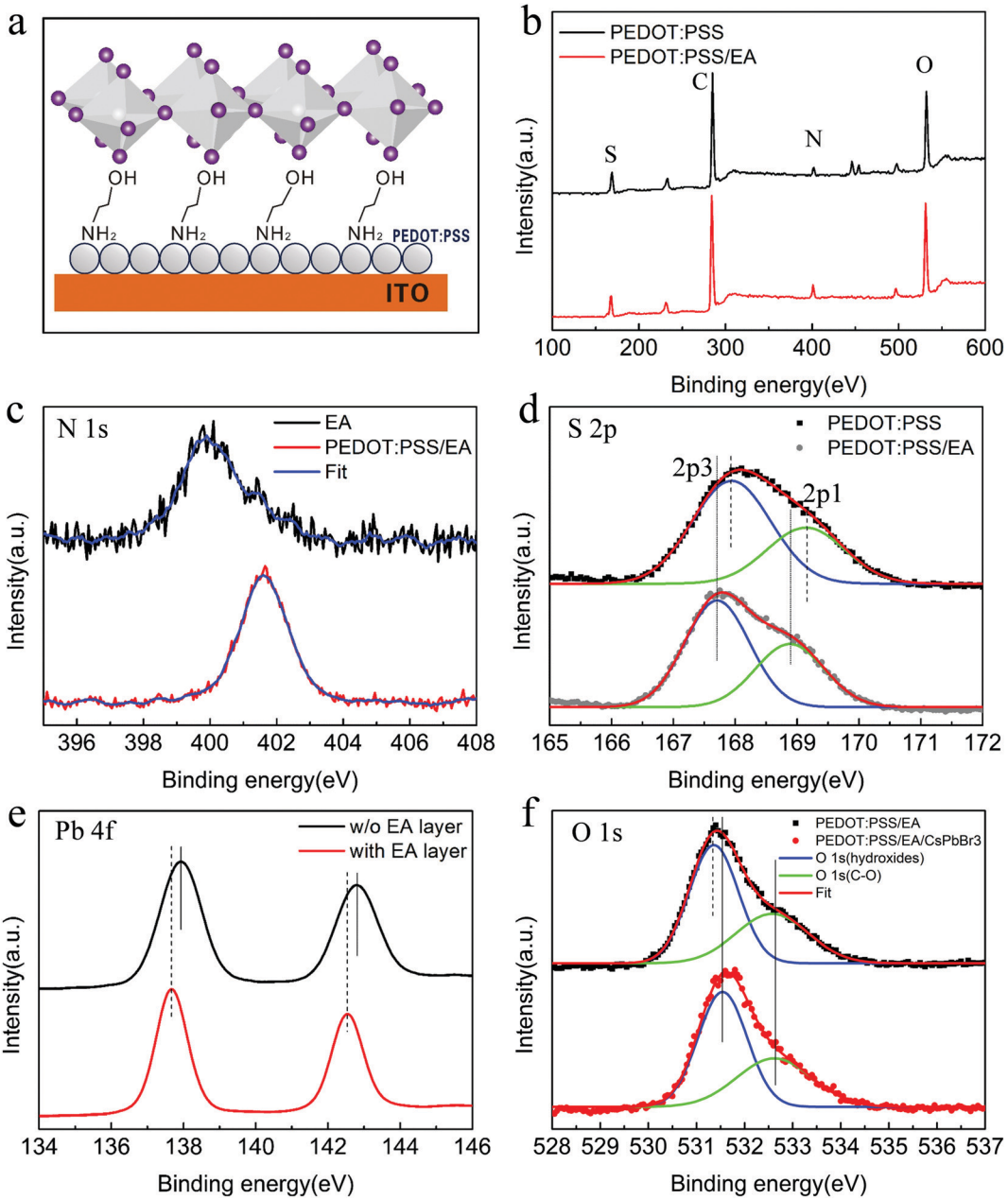

Fig. 4 (a) Schematic illustrations of PEDOT:PSS-EA-Perovskite. (b) XPS wide spectra of PEDOT:PSS and PEDOT:PSS/EA. (c) XPS spectra of N 1s for EA and PEDOT:PSS/EA. (d) XPS spectra of S 2p for PEDOT:PSS and PEDOT:PSS/EA. (e) XPS spectra of Pb 4f for PEDOT:PSS/$CsPbBr_3$ and PEDOT:PSS/EA/$CsPbBr_3$. (f) XPS spectra of O 1s for PEDOT:PSS/EA and PEDOT:PSS/EA/$CsPbBr_3$.

to determine the chemical state of elements and analyze the interaction between functional groups, as shown in Fig. 4b–e. Fig. 4b presents the XPS spectra of PEDOT:PSS and PEDOT:PSS/EA films. It can be seen from the figure that the nitrogen element is detected in PEDOT:PSS, which is caused by the adsorption of nitrogen in the air. After using EA, the peak position of the N 1s peak is obviously enhanced, indicating that EA has been deposited on the surface of PEDOT:PSS. Meanwhile, the N 1s peak shows a shift by 1.55 eV towards high binding energy (Fig. 4c), which reveals that electrons are lost from EA at the interface.[62,63] Then, we analyzed the XPS high-resolution spectrum signal of the sulfur element. Compared with the pure PEDOT: PSS film, the addition of an EA interface layer made the S 2p peak move to the low binding energy (BE), as shown in Fig. 4d. The decrease of binding energy of S 2p indicated that the electron density around the sulfur atom increased by obtaining electrons.[64] The above results illustrate that EA spin-coated on the PEDOT:PSS film promoted the information of Lewis acid–base complexes by reaction between the amine groups of EA and sulfonyl groups in the PEDOT:PSS film. At this time, the hydrophilic hydroxyl groups exposed on the surface of the interface layer did not participate in any reaction, which would be beneficial to the bonding of perovskite grains on the EA layer and improve the wettability of the perovskite layer. So the further analysis of the interaction between EA interface layer and perovskite layer was also carried out by XPS. Fig. 4e shows the XPS spectra of Pb 4f peaks in the perovskite film with or without EA layer. Fig. 4f displays the XPS spectra of O 1s in EA with or without the $CsPbBr_3$ layer, in which two peaks at approximately 531.5 and 532.6 eV were fitted, which are attributed to the C–O single bond and the hydroxide bond, respectively.[14,65] Addition of the EA interface layer made the binding energy of Pb 4f decrease by 0.2 eV, while the O 1s peaked at low BE presented a redshift of 0.2 eV after the deposition of the $CsPbBr_3$ layer, indicating the coordination reaction between lead and hydroxyl groups.[65] At the same time, the C–O double bond and Br 3d (Fig. S10, ESI†) did not change.[42] In order to verify whether the amine groups in the EA layer will coordinate with the lead ions in perovskite, PEDOT:PSS/$CsPbBr_3$ and PEDOT:PSS/EA/$CsPbBr_3$ were analyzed by XPS (Fig. S11, ESI†). It can be found that the N 1s peak shows no significant change after EA inserted. Therefore, it can be deduced that the lead ions in perovskite would be fastened to the hydroxyl groups at the interface to induce $CsPbBr_3$ nucleation and growth. Moreover, the interactions at PEDOT:PSS/EA and EA/$CsPbBr_3$ interfaces would form two dipoles that are both directed toward the emissive layer, which would promote the injection and transport of holes at the anode, further promoting the EL performance of PeLEDs.

Conclusions

In summary, an ampholytic interface EA was introduced into the $CsPbBr_3$ based PeLEDs to induce grain nucleation and growth; meanwhile a passivator T80 was employed in the bulk $CsPbBr_3$ film to suppress the non-radiative defects at the grain boundaries. Under the synergistic effect of interface modification and defect passivation, an efficient PeLED was obtained with a maximum brightness of 50 900 cd m^{-2}, a maximum CE of 44.32 cd A^{-1}, and a maximum EQE of 12.7%. The mechanism of the effect of EA interface has been investigated in detail, which revealed that the EA can interact with both PEDOT:PSS and $CsPbBr_3$ together, inducing $CsPbBr_3$ grain nucleation and growth, and obtaining a compact and uniform film morphology. Besides this, the formed dipoles by inserting EA are also conducive to the injection and transport of holes at the anode, thus boosting the PeLED performance. This work would provide a meaningful strategy and mechanism for the *in situ* morphology control of perovskite films, and developing PeLEDs with high efficiency.

Experimental

Materials

Lead bromide, PEDOT:PSS and TPBi were purchased from Xi'an Polymer Light Technology Corp. Cesium bromide was purchased from Kanto Chemical Co., Ltd T80 and EA were purchased from Sigma-Aldrich. All materials were used directly without further purification.

Perovskite film fabrication and characterization

The powders of cesium bromide and lead bromide (molar ratio of 1.86 : 1) were added into an anhydrous dimethylsulfoxide (DMSO) solvent containing T80 and stirred at 50 °C for 4 hours. A transparent perovskite precursor solution with a concentration of 145 mg ml^{-1} was obtained. The concentrations of T80 in DMSO were 1, 3, 5, 7 and 9 mg ml^{-1}, respectively. In this experiment, perovskite thin films were prepared *via* spin-coating method: 100 μl $CsPbBr_3$ precursor solution was dropped on the center of the substrate. The perovskite films were obtained by spin-coating at 4500 rpm for 60 s. Then the samples were heated at 70 °C for 10 min to improve the crystallization. The morphology of $CsPbBr_3$ thin films was characterized by SEM (Hitachi 4800). The surface roughness was analyzed by AFM on a Shimadzu SPA-9700. The absorption spectra of $CsPbBr_3$ thin films were measured on a Shimadzu UV-3101PC. The PL spectra of $CsPbBr_3$ thin films were measured using a Hitachi F-7000 fluorescence spectrometer. Time-resolved PL spectra of $CsPbBr_3$ thin films were measured on an Edinburgh FLS920 spectrometer. XPS spectra were acquired by Escalab 250. The XRD patterns of perovskite films were measured using Rigaku SmartLab.

Device fabrication and characterization

The device structure of perovskite light-emitting diode mainly includes the following sections: ITO/PEDOT:PSS/EA/$CsPbBr_3$/TPBi/Bphen/Cs_2CO_3/Ag. Before use the ITO electrode was cleaned ultrasonically with acetone, ethanol and deionized water for 20 minutes each time, and then treated in an ultraviolet ozone environment for 15 minutes. Solution of PEDOT:PSS before use was filtered with 0.22 μm water-based filter head to remove large particles and insoluble substances. The EA was dissolved ethanol to form a solution with different volume

concentrations (5%, 10%, 20%, and 40%). Then the ITO electrode treated with UVO is placed on the tray of the homogenizer, and a filtered solution of PEDOT:PSS was dropped on the filtered ITO electrode. PEDOT:PSS thin films were obtained by spin-coating at 2500 rpm for 40 s. The substrate was then placed on a 140 °C hot stage for 15 min. After annealing, the EA layer was prepared under the same experimental conditions. Then, the substrates were transferred to a glove box filled with nitrogen to prepare perovskite films. TPBi (40 nm), Bphen (10 nm), Cs_2CO_3 (1 nm) and Ag (100 nm) are successively evaporated in a thermal evaporation equipment with a vacuum of 5.0×10^{-5} Pa. The evaporation rates are 1, 1, 0.5 and 4 Hz s^{-1}, respectively. Among them, the ultra-thin Cs_2CO_3 film can adjust the work function of the Ag electrode, so that the work function of the Ag electrode can be better matched with the lowest unoccupied molecular orbital (LUMO) of the electron transport layer. The effective area of PeLEDs was 0.04 cm^2. The current density–voltage curve and luminance–voltage curve of the device were measured by using a Keithley 2611 digital source meter and a luminance meter (Konica-Minolta LS-110). The EL spectrum of the device was measured using an optical fiber spectrometer. EQE is calculated based on the brightness, current and the emission spectrum of the hypothetical Lambert emission. All tests were carried out in air and without encapsulation.

Conflicts of interest

There are no conflicts to declare.

Acknowledgements

This work is supported by the National Science Foundation of China No. 61774154, 61875195, 61975256, 51973208, and 62035013, the Jilin Province Science and Technology Research Project No. 20180201029GX, 20190302084GX, and 20190302087GX, and the Project supported by the Dawn Talent Training Program of CIOMP.

Notes and references

1 N. Wang, L. Cheng, R. Ge, S. Zhang, Y. Miao, W. Zou, C. Yi, Y. Sun, Y. Cao, R. Yang, Y. Wei, Q. Guo, Y. Ke, M. Yu, Y. Jin, Y. Liu, Q. Ding, D. Di, L. Yang, G. Xing, H. Tian, C. Jin, F. Gao, R. H. Friend, J. Wang and W. Huang, *Nat. Photonics*, 2016, **10**, 699–704.
2 Y. H. Kim, H. Cho, J. H. Heo, T. S. Kim, N. Myoung, C. L. Lee, S. H. Im and T. W. Lee, *Adv. Mater.*, 2015, **27**, 1248–1254.
3 S. D. Stranks, G. E. Eperon, G. Grancini, C. Menelaou, M. J. P. Alcocer, T. Leijtens, L. M. Herz, A. Petrozza and H. J. Snaith, *Science*, 2013, **342**, 341–344.
4 G. C. Xing, N. Mathews, S. Y. Sun, S. S. Lim, Y. M. Lam, M. Gratzel, S. Mhaisalkar and T. C. Sum, *Science*, 2013, **342**, 344–347.
5 C. Wehrenfennig, G. E. Eperon, M. B. Johnston, H. J. Snaith and L. M. Herz, *Adv. Mater.*, 2014, **26**, 1584–1589.
6 Z. Li, Z. Chen, Y. Yang, Q. Xue, H. L. Yip and Y. Cao, *Nat. Commun.*, 2019, **10**, 1027.
7 X. Yang, X. Zhang, J. Deng, Z. Chu, Q. Jiang, J. Meng, P. Wang, L. Zhang, Z. Yin and J. You, *Nat. Commun.*, 2018, **9**, 570.
8 W. Xu, Y. Gao, W. Ming, F. He, J. Li, X. H. Zhu, F. Kang, J. Li and G. Wei, *Adv. Mater.*, 2020, e2003965.
9 Q. Hu, W. Chen, W. Yang, Y. Li, Y. Zhou, B. W. Larson, J. C. Johnson, Y.-H. Lu, W. Zhong, J. Xu, L. Klivansky, C. Wang, M. Salmeron, A. B. Djurišić, F. Liu, Z. He, R. Zhu and T. P. Russell, *Joule*, 2020, **4**, 1575–1593.
10 D. J. Wu, H. Zhou, S. Zehao, M. Zheng, R. H. Liu, X. Y. Pan, H. Z. Wan, J. Zhang, H. Wang, X. M. Li and H. B. Zeng, *ACS Nano*, 2020, **14**, 2777–2787.
11 C. H. Kang, I. Dursun, G. Y. Liu, L. Sinatra, X. B. Sun, M. W. Kong, J. Pan, P. Maity, E. N. Ooi, T. K. Ng, O. F. Mohammed, O. M. Bakr and B. S. Ooi, *Light: Sci. Appl.*, 2019, **8**, 94.
12 L. Gu and Z. Fan, *Light: Sci. Appl.*, 2017, **6**, e17090.
13 Y. F. Miao, L. Cheng, W. Zou, L. H. Gu, J. Zhang, Q. Guo, Q. M. Peng, M. M. Xu, Y. R. He, S. T. Zhang, Y. Cao, R. Z. Li, N. N. Wang, W. Huang and J. P. Wang, *Light: Sci. Appl.*, 2020, **9**, 89.
14 X. Liu, X. Y. Guo, Y. Lv, Y. S. Hu, Y. Fan, J. Lin, X. M. Liu and X. Y. Liu, *Adv. Opt. Mater.*, 2018, **6**, 1801245.
15 C. J. Qin, A. S. D. Sandanayaka, C. Y. Zhao, T. Matsushima, D. Z. Zhang, T. Fujihara and C. Adachi, *Nature*, 2020, **585**, 53–57.
16 F. Yan, S. T. Tan, X. Li and H. V. Demir, *Small*, 2019, **15**, 1902079.
17 Q. Liao, X. Jin and H. B. Fu, *Adv. Opt. Mater.*, 2019, **7**, 1900099.
18 K. Wang, Y. Du, J. Liang, J. Zhao, F. F. Xu, X. Liu, C. Zhang, Y. Yan and Y. S. Zhao, *Adv. Mater.*, 2020, **32**, e2001999.
19 Z. K. Gu, Z. D. Huang, X. T. Hu, Y. Wang, L. H. Li, M. Z. Li and Y. L. Song, *ACS Appl. Mater. Interfaces*, 2020, **12**, 22157–22162.
20 Z. Gu, Z. Zhou, Z. Huang, K. Wang, Z. Cai, X. Hu, L. Li, M. Li, Y. S. Zhao and Y. Song, *Adv. Mater.*, 2020, **32**, 1908006.
21 Z. K. Tan, R. S. Moghaddam, M. L. Lai, P. Docampo, R. Higler, F. Deschler, M. Price, A. Sadhanala, L. M. Pazos, D. Credgington, F. Hanusch, T. Bein, H. J. Snaith and R. H. Friend, *Nat. Nanotechnol.*, 2014, **9**, 687–692.
22 K. B. Lin, J. Xing, L. N. Quan, F. P. G. de Arquer, X. W. Gong, J. X. Lu, L. Q. Xie, W. J. Zhao, D. Zhang, C. Z. Yan, W. Q. Li, X. Y. Liu, Y. Lu, J. Kirman, E. H. Sargent, Q. H. Xiong and Z. H. Wei, *Nature*, 2018, **562**, 245–248.
23 Y. Cao, N. Wang, H. Tian, J. Guo, Y. Wei, H. Chen, Y. Miao, W. Zou, K. Pan, Y. He, H. Cao, Y. Ke, M. Xu, Y. Wang, M. Yang, K. Du, Z. Fu, D. Kong, D. Dai, Y. Jin, G. Li, H. Li, Q. Peng, J. Wang and W. Huang, *Nature*, 2018, **562**, 249–253.
24 L. Zhang, F. Yuan, J. Xi, B. Jiao, H. Dong, J. R. Li and Z. X. Wu, *Adv. Funct. Mater.*, 2020, **30**, 2001834.
25 Y. F. Miao, Y. Ke, N. N. Wang, W. Zou, M. M. Xu, Y. Cao, Y. Sun, R. Yang, Y. Wang, Y. F. Tong, W. J. Xu, L. D. Zhang, R. Z. Li, J. Li, H. P. He, Y. Z. Jin, F. Gao, W. Huang and J. P. Wang, *Nat. Commun.*, 2019, **10**, 3624.
26 W. Xu, Q. Hu, S. Bai, C. Bao, Y. Miao, Z. Yuan, T. Borzda, A. J. Barker, E. Tyukalova, Z. Hu, M. Kawecki, H. Wang, Z. Yan, X. Liu, X. Shi, K. Uvdal, M. Fahlman, W. Zhang,

M. Duchamp, J.-M. Liu, A. Petrozza, J. Wang, L.-M. Liu, W. Huang and F. Gao, *Nat. Photonics*, 2019, **13**, 418–424.
27 H. R. Wang, X. Y. Zhang, Q. Q. Wu, F. Cao, D. W. Yang, Y. Q. Shang, Z. J. Ning, W. Zhang, W. T. Zheng, Y. F. Yan, S. V. Kershaw, L. J. Zhang, A. L. Rogach and X. Y. Yang, *Nat. Commun.*, 2019, **10**, 665.
28 L.-P. Cheng, J.-S. Huang, Y. Shen, G.-P. Li, X.-K. Liu, W. Li, Y.-H. Wang, Y.-Q. Li, Y. Jiang, F. Gao, C.-S. Lee and J.-X. Tang, *Adv. Opt. Mater.*, 2019, **7**, 1801534.
29 J. X. Zhong, W. Q. Wu, J. F. Liao, W. H. Feng, Y. Jiang, L. Z. Wang and D. B. Kuang, *Adv. Energy Mater.*, 2020, **10**, 1902256.
30 Y. Jin, S. Yuan, K.-L. Wang, M. Li, Q. Wang, Z.-K. Wang and L.-S. Liao, *Appl. Phys. Lett.*, 2019, **114**, 163302.
31 Z. W. Ren, X. T. Xiao, R. M. Ma, H. Lin, K. Wang, X. W. Sun and W. C. H. Choy, *Adv. Funct. Mater.*, 2019, **29**, 1905339.
32 C. H. Mak, X. Y. Huang, R. G. Liu, Y. Q. Tang, X. Han, L. Ji, X. L. Zou, G. Z. Zou and H. Y. Hsu, *Nano Energy*, 2020, **73**, 104752.
33 B. Chen, P. N. Rudd, S. Yang, Y. Yuan and J. Huang, *Chem. Soc. Rev.*, 2019, **48**, 3842–3867.
34 Z. C. Yuan, Y. F. Miao, Z. J. Hu, W. D. Xu, C. Y. Kuang, K. Pan, P. L. Liu, J. Y. Lai, B. Q. Sun, J. P. Wang, S. Bai and F. Gao, *Nat. Commun.*, 2019, **10**, 2818.
35 B. N. Han, S. C. Yuan, T. Fang, F. J. Zhang, Z. F. Shi and J. Z. Song, *ACS Appl. Mater. Interfaces*, 2020, **12**, 14224–14232.
36 L. Xu, J. Li, B. Cai, J. Song, F. Zhang, T. Fang and H. Zeng, *Nat. Commun.*, 2020, **11**, 3902.
37 P. Schulz, D. Cahen and A. Kahn, *Chem. Rev.*, 2019, **119**, 3349–3417.
38 T. H. Han, S. Tan, J. Xue, L. Meng, J. W. Lee and Y. Yang, *Adv. Mater.*, 2019, e1803515.
39 J. E. Jeong, J. H. Park, C. H. Jang, M. H. Song and H. Y. Woo, *Adv. Mater.*, 2020, e2002176.
40 T. Zhang, M. Long, L. Pan, K. Ngai, M. Qin, F. Xie, X. Lu, J. Chen and J. Xu, *Sci. Bull.*, 2020, **65**, 1832–1839.
41 M. Y. Ban, Y. T. Zou, J. P. H. Rivett, Y. G. Yang, T. H. Thomas, Y. S. Tan, T. Song, X. Y. Gao, D. Credington, F. Deschler, H. Sirringhaus and B. Q. Sun, *Nat. Commun.*, 2018, **9**, 3892.
42 B. Zhao, Y. Lian, L. Cui, G. Divitini, G. Kusch, E. Ruggeri, F. Auras, W. Li, D. Yang, B. Zhu, R. A. Oliver, J. L. MacManus-Driscoll, S. D. Stranks, D. Di and R. H. Friend, *Nat. Electron.*, 2020, **3**, 704–710.
43 J. Wang, N. Wang, Y. Jin, J. Si, Z. K. Tan, H. Du, L. Cheng, X. Dai, S. Bai, H. He, Z. Ye, M. L. Lai, R. H. Friend and W. Huang, *Adv. Mater.*, 2015, **27**, 2311–2316.
44 B. Zhao, S. Bai, V. Kim, R. Lamboll, R. Shivanna, F. Auras, J. M. Richter, L. Yang, L. Dai, M. Alsari, X.-J. She, L. Liang, J. Zhang, S. Lilliu, P. Gao, H. J. Snaith, J. Wang, N. C. Greenham, R. H. Friend and D. Di, *Nat. Photonics*, 2018, **12**, 783–789.
45 Y. Ling, Z. Yuan, Y. Tian, X. Wang, J. C. Wang, Y. Xin, K. Hanson, B. Ma and H. Gao, *Adv. Mater.*, 2016, **28**, 305–311.
46 L. Tang, J. Qiu, Q. Wei, H. Gu, B. Du, H. Du, W. Hui, Y. Xia, Y. Chen and W. Huang, *ACS Appl. Mater. Interfaces*, 2019, **11**, 29132–29138.
47 Y. Shen, M. N. Li, Y. Q. Li, F. M. Xie, H. Y. Wu, G. H. Zhang, L. Chen, S. T. Lee and J. X. Tang, *ACS Nano*, 2020, **14**, 6107–6116.
48 R. Fan, L. Song, Y. Hu, X. Guo, X. Liu, L. Wang, C. Geng, S. Xu, Y. Zhang, Z. Zhang, N. Luan and W. Bi, *ACS Appl. Mater. Interfaces*, 2020, **12**, 43331–43338.
49 K. Sim, T. Jun, J. Bang, H. Kamioka, J. Kim, H. Hiramatsu and H. Hosono, *Appl. Phys. Rev.*, 2019, **6**, 031402.
50 S. Lee, D. B. Kim, I. Hamilton, M. Daboczi, Y. S. Nam, B. R. Lee, B. Zhao, C. H. Jang, R. H. Friend, J. S. Kim and M. H. Song, *Adv. Sci.*, 2018, **5**, 1801350.
51 C. F. Huang, M. L. Keshtov and F. C. Chen, *ACS Appl. Mater. Interfaces*, 2016, **8**, 27006–27011.
52 Y. Zou, M. Ban, Y. Yang, S. Bai, C. Wu, Y. Han, T. Wu, Y. Tan, Q. Huang, X. Gao, T. Song, Q. Zhang and B. Sun, *ACS Appl. Mater. Interfaces*, 2018, **10**, 24320–24326.
53 L. Q. Zhang, X. L. Yang, Q. Jiang, P. Y. Wang, Z. G. Yin, X. W. Zhang, H. R. Tan, Y. Yang, M. Y. Wei, B. R. Sutherland, E. H. Sargent and J. B. You, *Nat. Commun.*, 2017, **8**, 15640.
54 Y. Liu, J. Y. Cui, K. Du, H. Tian, Z. F. He, Q. H. Zhou, Z. L. Yang, Y. Z. Deng, D. Chen, X. B. Zuo, Y. Ren, L. Wang, H. M. Zhu, B. D. Zhao, D. W. Di, J. P. Wang, R. H. Friend and Y. Z. Jin, *Nat. Photonics*, 2019, **13**, 760–764.
55 W. Q. Wu, J. F. Liao, J. X. Zhong, Y. F. Xu, L. Wang and J. Huang, *Angew. Chem., Int. Ed.*, 2020, **59**, 2–10.
56 Q. Peng, J. Guo, Q. Zhang, J. Xiang, B. Liu, A. Zhou, R. Liu and Y. Tian, *J. Am. Chem. Soc.*, 2014, **136**, 4113–4116.
57 Y. Tian, C. Zhou, M. Worku, X. Wang, Y. Ling, H. Gao, Y. Zhou, Y. Miao, J. Guan and B. Ma, *Adv. Mater.*, 2018, **30**, e1707093.
58 H. Wang, F. U. Kosasih, H. Yu, G. Zheng, J. Zhang, G. Pozina, Y. Liu, C. Bao, Z. Hu, X. Liu, L. Kobera, S. Abbrent, J. Brus, Y. Jin, M. Fahlman, R. H. Friend, C. Ducati, X. K. Liu and F. Gao, *Nat. Commun.*, 2020, **11**, 891.
59 Y. Bai, H. Chen, S. Xiao, Q. Xue, T. Zhang, Z. Zhu, Q. Li, C. Hu, Y. Yang, Z. Hu, F. Huang, K. S. Wong, H.-L. Yip and S. Yang, *Adv. Funct. Mater.*, 2016, **26**, 2950–2958.
60 A. A. Zhumekenov, M. I. Saidaminov, M. A. Haque, E. Alarousu, S. P. Sarmah, B. Murali, I. Dursun, X.-H. Miao, A. L. Abdelhady, T. Wu, O. F. Mohammed and O. M. Bakr, *ACS Energy Lett.*, 2016, **1**, 32–37.
61 Q. Huang, Y. Zou, S. Bourelle, T. Zhai, T. Wu, Y. Tan, Y. Li, J. Li, S. Duhm, T. Song, L. Wang, F. Deschler and B. Sun, *Nanoscale Horiz.*, 2019, **4**, 924–932.
62 A. Radi and K. T. Leung, *Mater. Express*, 2011, **1**, 144–153.
63 J. C. Yu, D. B. Kim, G. Baek, B. R. Lee, E. D. Jung, S. Lee, J. H. Chu, D. K. Lee, K. J. Choi, S. Cho and M. H. Song, *Adv. Mater.*, 2015, **27**, 3492–3500.
64 W. Song, X. Fan, B. Xu, F. Yan, H. Cui, Q. Wei, R. Peng, L. Hong, J. Huang and Z. Ge, *Adv. Mater.*, 2018, **30**, e1800075.
65 Y. N. Wu, L. H. Liu, W. Wang, W. Z. Zhang, H. T. Yu, J. Qian, Y. F. Chen, W. Shen, S. Q. Sui, Z. T. Deng, S. F. Chen and W. Huang, *J. Mater. Chem. C*, 2020, **8**, 9936–9944.